

Conformal Surface Registration with Applications on Face Morphing

MEI-HENG YUEH , XIANFENG DAVID GU , WEN-WEI LIN ,
CHIN-TIEN WU AND SHING-TUNG YAU

Morphing is the process of changing a geometric model or an image into another. The process generally involves rigid body motions and non-rigid deformations. It is well known that there exists a unique conformal mapping from a simply connected surface into a unit disk by the Riemann mapping theorem. On the other hand, a 3D surface deformable model can be built via various approaches such as mutual parameterization from direct interpolation or surface matching using landmarks. In this paper, a numerical methods of 3D surface morphing based on deformable model and conformal mapping is demonstrated. We take the advantage of the unique representation of 3D surfaces by the mean curvatures H and the conformal factors λ associated with the Riemann mapping and build up the deformation model by consistently registering the landmarks on the conformal parametric domains. As a result, the correspondence of the (H, λ) between two surfaces can be defined and a 3D deformation field can be reconstructed. Furthermore, by composition of the Möbius transformation and the 3D deformation field, a smooth morphing sequence can be generated over a consistent mesh structure via the cubic spline homotopy. Several numerical experiments on the face morphing are presented to demonstrate the robustness of our approach.

KEYWORDS AND PHRASES: conformal mapping, surface morphing, surface registration.

1. Introduction

The metamorphosis between two objects is commonly called *morphing*. It is the process of changing a geometric model or an image into another. In this paper, we consider surface morphing: the morphing between two surfaces in \mathbb{R}^3 . Thanks to the advance of the three-dimensional image scanning technology, the geometric and the texture information of a surface can be easily obtained by scanners and image morphing techniques in 3D have recently

attracted more attentions in the fields of image registration and digital animation, etc. However, even though 2D image morphing technique has pretty matured, 3D image morphing remains challenging, especially, when realistic morphing effects are desired. To achieve a realistic 3D facial morphing effects, Decarlo et al. [9] introduced an anthropometric face model using variational techniques, Obaid et al. [28] proposed a quadratic deformation model based on MPEG-4 animation standard, Mattos et al. [26] employed a model driven approach based on structure registration, and Yang et al. [35] propose a morphing target method in which realistic textures can be rendered on a digital model in real time.

The main challenge in 3D surface morphing is that not only important geometric features shall be kept in the morphing process, but also the texture images need to be generated with high accuracy and quality in order to achieve a satisfactory visual effect. Technically, the difficulties arise due to (i) lack of consistent meshes between two surfaces, (ii) ambiguous correspondence between interpolated geometry and texture and (iii) expensive cost in computing a smooth 3D deformation path. For creating consistent meshes, the process of landmarks selection is not only time consuming, but also subjected to manual error. Various automatic landmark selection algorithms are developed. For example, Lipman and Funkhouser [22] proposed an automatic algorithm for finding surface correspondences by using conformal flattening and Möbius transformations. Zanella et al. [36] use the so-called *Active Shape Models* [8] to find the facial features. For creating geometrically consistent texture mapping, Guo et al. [18] proposed a landmark-based morphing technique to render the surface light fields of the objects in the morphing sequence based on spherical embedding of meshes. Kurtek et al. [20] developed a framework for computing full correspondence between two surfaces by using a constrained optimization with a sparse set of landmarks. Ma et al. [25] proposed a multi-scales polynomial deformation map to synthesize facial performance with dynamic wrinkles and fine scale facial details. In this work, we simply assume the landmarks are prescribed on the given surfaces and render the texture of the interpolated images based on Guo's light field blending. We shall focus on computing a smooth 3D deformation path which preserves geometrical features with high accuracy and quality. Since the deformation field is mainly determined by surface registration: finding the spatial correspondence of two surfaces. We briefly review some of the techniques that is related to this key issues in the following.

Many techniques have been developed to achieve a desired morphing effect in 2D. *Warping* [30, 33, 34] via finding the correspondence between two

images is one of the classical techniques. By partitioning each image into several blocks based on a given set of landmarks, the correspondence between each pair of blocks can be obtained by a local transformation such as affine or polynomial mappings, etc. Inspired by the warping method, Lee et al. proposed a technique, called *deformable surface model* [21], that generates a C^1 -continuous and one-to-one deformation from matching a set of positional constraints, hereafter called landmarks, in the given two-dimensional images. The transition behavior can also be controlled by assigning transition curves for selected points on an image. Similarly, Bookstein proposed the *thin-plate spline* model (TPS) [3] for landmarks registration in which the deformation is controlled by the biharmonic basis functions. To deal with large deformation occurs in landmark matching, Camion and Younes [4], proposed to compute the geodesic spline via a diffeomorphism in which a prescribed elastic energy is minimized. Younes et al. further applied the method to match the magnetic resonance images (MRIs) and the method is known as the *large deformation diffeomorphic metric mapping* (LDDMM) [5] in the field of MRIs' registration. For preserving local properties of 2D images during the morph, recently, Chen et al. [6] proposed a shape interpolation scheme by using conformal deformations.

The warping technique can be naturally extended to surfaces in \mathbb{R}^3 . A geometrical morphing method is proposed by Gregory et al. [12] where landmarks on each surface are connected to form consistent meshes, surfaces are decomposed into several regions by the meshes, and then the correspondence between each pair of regions are obtained via harmonic mappings. Liu et al. [24] proposed a morphing method based on affine transformations and translations that works well even when two input 3D triangle meshes have very different shapes. The morph can be made more realistic by constructing the morphing path based on physical laws which characterizes the intrinsic deformation of the surface. Verbeek et al. [32] and Bao et al. [1] proposed methods of determining the morphing paths by optimizing the bending energy and elastic strain energy, respectively, on a deformable closed surface. Schröder et al. [23] proposed a variational approach based on minimizing bending and stretching on the parameter domains in which corresponding landmarks and line segments are matched.

1.1. Contribution

In this study, we propose an efficient way to generate the warp of 3D human faces. First, we align and scale the 3D faces by applying the iterative closest point (ICP) algorithm on those landmark points that only subjected to

rigid motion. Next, conformal mappings are then used to parameterize the aligned 3D surfaces. With the help of the unique conformal representation (H, λ) of surfaces, instead of computing a three dimensional deformation field, we compute the deformation field on the conformal parametric domain. A Möbius transformation and a deformation based on the landmark matching are computed to achieve high accurate landmark correspondence. The landmark points are selected according to the facial action codes in MPEG-4 [28] and a consistent mesh that connected those landmark points is created to control digital models so that the deformation path of one face can be transformed to another face. As a result, one can drive the face of a digital model via the facial performance of a real agent. A desired facial performance can also be obtained by morphing among given facial expressions via a smooth homotopy path of the deformation fields. In addition, our approach also allow video compression by combining the key frames extraction and standard JPEG compression on the images that associated with the mean curvature H and conformal factor λ .

In the following, we briefly review the computation of the Riemann conformal mapping and surface reconstruction by using the mean curvature and conformal factor in section 2. Then we present our surface registration technique in section 3 and introduce cubic spline homotopy in section 4. After that, we demonstrate some morphing results in section 5.

2. Surface parameterization and reconstruction

The Riemann conformal mapping plays an important role in the surface parameterization. The following celebrated *Riemann mapping theorem* guarantees the existence of such mapping.

Theorem 2.1 (Uniformization theorem). *[29, 11, 19] Suppose $\overline{\mathcal{M}}$ is a closed Riemann surface of genus zero. Then there exists a conformal diffeomorphism $\varphi : \overline{\mathcal{M}} \rightarrow \mathbb{S}^2$ that maps $\overline{\mathcal{M}}$ onto the unit sphere \mathbb{S}^2 .*

In this section, we briefly review the numerical algorithm for computing Riemann conformal mapping.

2.1. Conformal parameterization

The spherical conformal mapping, illustrated in Figure 1, is first computed by Gu and Yau [15] in 2003. The idea is based on minimizing the harmonic energy through a nonlinear heat diffusion process as following: Suppose the desired map is $\varphi : \overline{\mathcal{M}} \rightarrow \mathbb{S}^2$. Let $\varphi(v)$ and $\mathbf{n}(\varphi(v))$ denote the image of the

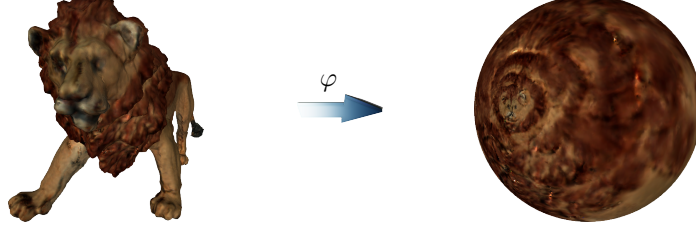


Figure 1: An illustration of the spherical conformal mapping that maps a closed surface of a lion onto a unit sphere.

vertex $v \in \overline{\mathcal{M}}$ and the normal at $\varphi(v)$, respectively. The normal and tangent components of $\Delta\varphi$ are defined as

$$(\Delta\varphi(v))^\perp = \langle \Delta\varphi(v), \mathbf{n}(\varphi(v)) \rangle \mathbf{n}(\varphi(v))$$

and

$$(\Delta\varphi(v))^\parallel = \Delta\varphi(v) - (\Delta\varphi(v))^\perp,$$

respectively. The harmonic map is then computed by minimizing the harmonic energy associated with φ through the nonlinear heat diffusion process

$$\frac{d\varphi}{dt} = -(\Delta\varphi)^\parallel,$$

with the constraint $\varphi(\overline{\mathcal{M}}, t) \in \mathbb{S}^2$. The equation can be rewritten in the following form,

$$\begin{aligned} \frac{d\varphi}{dt} &= -(\Delta\varphi)^\parallel \\ &= -(\Delta\varphi - \langle \Delta\varphi, \mathbf{n}(\varphi) \rangle \mathbf{n}(\varphi)) \\ &= -(\Delta\varphi - \langle \Delta\varphi, \varphi \rangle \varphi), \end{aligned}$$

discretized by linear finite element, and solved iteratively by using the quasi-implicit Euler method (QIEM) [13],

$$\left[I + \delta t^{(m)} (L - D^{(m)}) \right] \varphi^{(m+1)} = \varphi^{(m)},$$

where, L is the discrete Laplacian, $D^{(m)}$ is a diagonal matrix with

$$\left(D^{(m)} \right)_{ii} = \left\langle \left(L \varphi^{(m)} \right) (v_i), \varphi^{(m)} (v_i) \right\rangle.$$

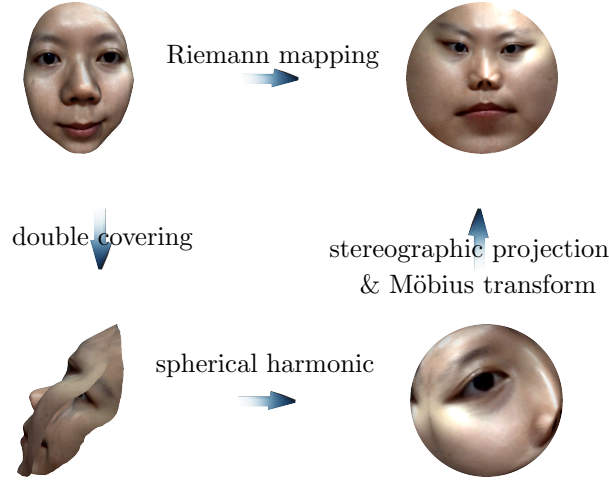


Figure 2: An illustration of the flow chart for computing the Riemann conformal mapping for an open surface.

The initial map $\varphi^{(0)}$ for the above iterative formula can be obtained from the *Gauss map*, which maps a vertex v to the unit surface normal $\mathbf{n}(v)$. It is known that the efficiency of the explicit scheme is usually not satisfactory since the time step is generally very small due to the diffusive nature. The quasi-implicit Euler method [13] proposed by Lin et al. is shown to be very robust on solving the nonlinear diffusion equation.

Remark. An open surface \mathcal{M} can be turned into a closed surface $\overline{\mathcal{M}}$ by double covering [17]. Then the closed surface $\overline{\mathcal{M}}$ can be mapped conformally onto a unit sphere \mathbb{S}^2 . After computing the spherical conformal mapping $\varphi : \overline{\mathcal{M}} \rightarrow \mathbb{S}^2$, we cut out the semi-sphere $\varphi(\mathcal{M})$ along the equator and map it onto the unit disk \mathbb{D} conformally by using the stereographic projection $\Pi_{\mathbb{S}}$, as shown in Figure 2. As a result, an open surface \mathcal{M} can be parameterized on \mathbb{D} conformally by $\Pi_{\mathbb{S}} \circ \varphi|_{\mathcal{M}} : \mathcal{M} \rightarrow \mathbb{D}$, which is known as the *Riemann mapping*. In the following, we denote the Riemann mapping by φ .

2.2. Surface reconstruction from Laplace-Beltrami equations

Let $(u_1, u_2) \in \mathbb{D}$ be a conformal parameterization of a surface \mathcal{M} . The metric on \mathcal{M} can be determined by its first fundamental form $ds^2 = \lambda(u_1, u_2)(du_1^2 + du_2^2)$, where $\lambda(u_1, u_2)$ represents the factor of stretching at the point (u_1, u_2) , which is known as the *conformal factor*. Theorem 2.2 in the following, proved

by Gu and Yau, states that any surface \mathcal{M} in \mathbb{R}^3 can be determined by its conformal factor λ and mean curvature H uniquely up to rigid motions [14, 16].

Theorem 2.2. (1) *A closed surface $\mathcal{M}(u_1, u_2)$ in \mathbb{R}^3 with conformal parameter (u_1, u_2) is determined by its conformal factor $\lambda(u_1, u_2)$ and its mean curvature $H(u_1, u_2)$ uniquely up to rigid motions.*
 (2) *A simply connected surface $\mathcal{M}(u_1, u_2)$ with a boundary in \mathbb{R}^3 with conformal parameter (u_1, u_2) is determined by its conformal factor $\lambda(u_1, u_2)$ and its mean curvature $H(u_1, u_2)$ and the boundary position.*

This theorem guarantees that one can define an operator $\Psi : \mathcal{R} \rightarrow C^2(\mathbb{D}) \times C^2(\mathbb{D})$ that maps a Riemann surface \mathcal{M} to its (H, λ) representation by

$$\Psi(\mathcal{M}) = (H, \lambda).$$

Here \mathcal{R} denotes the set of all the Riemann surfaces. Gu and Yau not only show that the operator Ψ is an one-to-one functional, but also the inversion of $\Psi(\mathcal{M})$ can be realized by solving the following Laplace-Beltrami equations

$$(1) \quad \begin{cases} \Delta_s \mathcal{M}(u_1, u_2) = 2H(u_1, u_2) \mathbf{n}(u_1, u_2) \\ \frac{\partial \mathcal{M}}{\partial u_1} \times \frac{\partial \mathcal{M}}{\partial u_2} = \lambda^2(u_1, u_2) \mathbf{n}(u_1, u_2) \mathcal{M}|_{\partial \mathbb{D}} \end{cases},$$

where

$$\Delta_s := \frac{1}{\lambda^2(u_1, u_2)} \left(\frac{\partial^2}{\partial u_1^2} + \frac{\partial^2}{\partial u_2^2} \right),$$

and $\mathbf{n}(u_1, u_2)$ is the normal of the surface \mathcal{M} . In other words, a unique surface \mathcal{M} in \mathbb{R}^3 can be reconstructed from the given mean curvature and the conformal factor (H, λ) . The detail algorithm for solving the Laplace-Beltrami equations can be seen in Algorithm 1.

2.3. Numerical results

In the following, for convenience, we abuse the notation to denote \mathcal{M} as the surface discretized by a triangular mesh. The discrete mean curvature H of the surface \mathcal{M} is computed by [27]

$$H(\mathbf{x}_i) = \frac{1}{4\text{Area}(N_1(\mathbf{x}_i))} \sum_{j \in N_1(\mathbf{x}_i)} (\cot \alpha_{ij} + \cot \alpha_{ji})(\mathbf{x}_i - \mathbf{x}_j) \cdot \mathbf{n},$$

Algorithm 1 Laplace-Beltrami Surface Reconstruction

Input: the mean curvature and the conformal factor (H, λ) of the surface \mathcal{M} and the boundary $\partial\mathcal{M}$ of the surface \mathcal{M} .

Output: the surface \mathcal{M} .

- 1: Set the initial surface normal $\mathbf{n}^{(0)}$.
- 2: **repeat**
- 3: Solve the boundary value problem

$$\Delta_s \mathcal{M}^{(j+1)} = 2H\lambda^2 \mathbf{n}^{(j)},$$

where boundary $\partial\mathcal{M}$ is known.

- 4: Update the surface normal

$$\mathbf{n}^{(j+1)} = \frac{\partial_{u_1} \mathcal{M}^{(j+1)} \times \partial_{u_2} \mathcal{M}^{(j+1)}}{\lambda^2}.$$

- 5: **until** convergence
-

where $N_1(\mathbf{x}_i)$ is the one-ring neighborhood of the vertex $\mathbf{x}_i \in \mathcal{M}$. The discrete conformal factor λ at x_i is computed by

$$\lambda(\mathbf{x}_i) = \frac{\text{Area}(N_1(\mathbf{x}_i))}{\text{Area}(\varphi(N_1(\mathbf{x}_i)))},$$

where φ is the Riemann conformal mapping. Then, by solving the equation (1), a reconstructed surface $\widehat{\mathcal{M}} := \Psi^{-1}(H, \lambda)$ can be obtained. In the following, we would like to check how close the reconstructed surface $\widehat{\mathcal{M}}$ is to the discrete surface \mathcal{M} . We call the error between the surface \mathcal{M} and the reconstructed surface $\widehat{\mathcal{M}}$ the *reconstruction error*. We compute the reconstruction error in L^1 -norm, L^2 -norm and L^∞ -norm as following,

$$\|\mathcal{M} - \widehat{\mathcal{M}}\|_1 := \frac{\iint_{\mathbb{D}} \|\mathcal{M}(u_1, u_2) - \widehat{\mathcal{M}}(u_1, u_2)\|_0 \left| \frac{\partial \varphi^{-1}}{\partial u_1} \wedge \frac{\partial \varphi^{-1}}{\partial u_2} \right| du_1 du_2}{\iint_{\mathbb{D}} \left| \frac{\partial \varphi^{-1}}{\partial u_1} \wedge \frac{\partial \varphi^{-1}}{\partial u_2} \right| du_1 du_2},$$

$$\|\mathcal{M} - \widehat{\mathcal{M}}\|_2 := \left(\frac{\iint_{\mathbb{D}} \|\mathcal{M}(u_1, u_2) - \widehat{\mathcal{M}}(u_1, u_2)\|_0^2 \left| \frac{\partial \varphi^{-1}}{\partial u_1} \wedge \frac{\partial \varphi^{-1}}{\partial u_2} \right| du_1 du_2}{\iint_{\mathbb{D}} \left| \frac{\partial \varphi^{-1}}{\partial u_1} \wedge \frac{\partial \varphi^{-1}}{\partial u_2} \right| du_1 du_2} \right)^{\frac{1}{2}},$$

and

$$\|\mathcal{M} - \widehat{\mathcal{M}}\|_\infty := \max_{(u_1, u_2) \in \mathbb{D}} \left\| \mathcal{M}(u_1, u_2) - \widehat{\mathcal{M}}(u_1, u_2) \right\|_0,$$

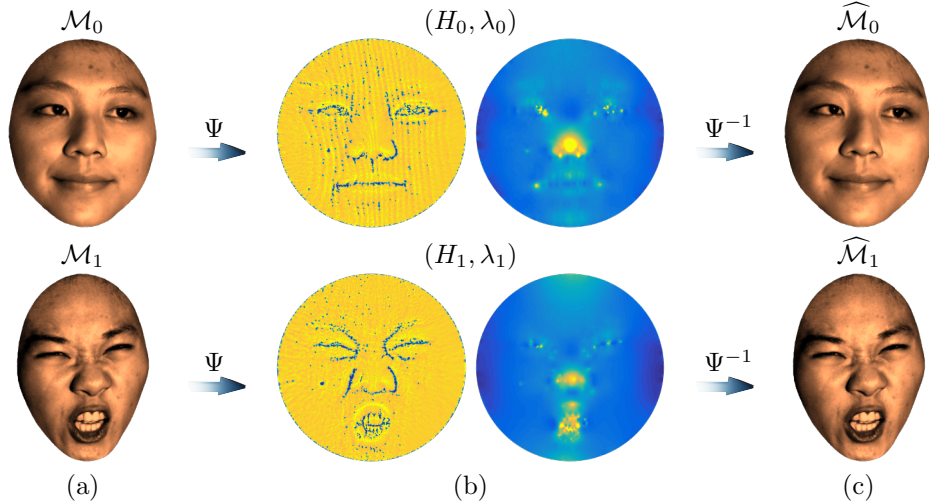


Figure 3: (a) The original surfaces of two human faces. (b) The mean curvature and the conformal factor of the original surfaces. (c) The reconstructed surfaces obtained from Algorithm 1.

respectively. Here $\|\cdot\|_0$ denotes the vector 2-norm in \mathbb{R}^3 .

The Riemann mapping of two different facial expressions, denoted by \mathcal{M}_0 and \mathcal{M}_1 , and the associated reconstructed surfaces are shown in Figure 3. The conformality of the numerical Riemann conformal mapping φ can be visualized via the angular change between a checkerboard pattern on \mathbb{D} and its image of the inverse map φ^{-1} on \mathcal{M} as illustrated in Figure 4 (a) and (b). We check whether the right angle at each corner point p of the checkerboard pattern is retained on the tangent plane $T_p\mathcal{M}$ by computing the angle distortion after the mapping. Figure 4 (c) shows the histograms of the angle distortion resulted from the numerical Riemann conformal map. Table 1 shows the reconstruction error in L^1 -norm, L^2 -norm and L^∞ -norm. Our numerical results indicate that the Riemann conformal map obtained by using QIEM algorithm preserves angle nicely and the surface reconstruction algorithm, Algorithm 1, indeed recovers the surface from its (H, λ) representation with a very small error.

3. Surface registration on parametric domain

For 3D surface registration, the positional and scaling differences of the images should be excluded. The scaling differences can be corrected by normalizing each surface using its diameter. The positional difference can be

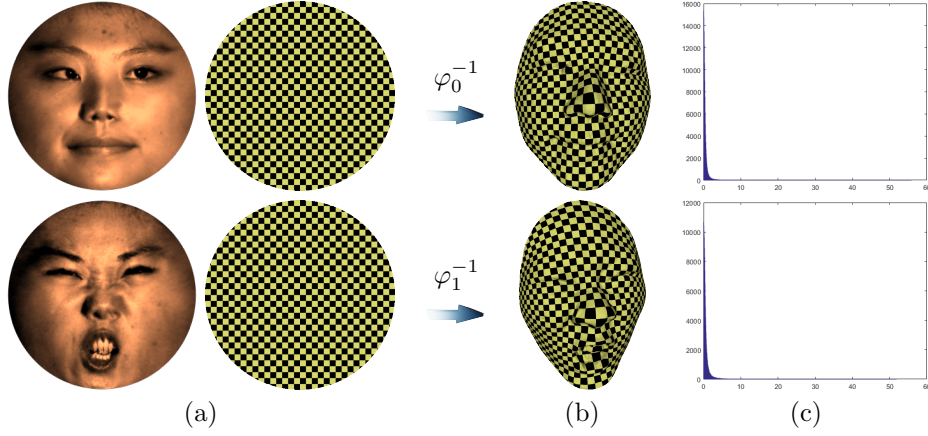


Figure 4: (a) The Riemann conformal mappings of two human faces and the checkerboard pattern. (b) The checkerboard pattern mapped by the inverse of the Riemann conformal mapping. (c) Histograms of the angle distortions of the Riemann conformal mappings.

relative reconstruction error	error measurement	L^1 -norm	L^2 -norm	L^∞ -norm
	$\ \mathcal{M}_0 - \widehat{\mathcal{M}}_0\ $		5.5775×10^{-3}	6.7193×10^{-3}
$\ \mathcal{M}_1 - \widehat{\mathcal{M}}_1\ $		1.9626×10^{-3}	2.4743×10^{-3}	2.0737×10^{-2}

Table 1: The relative reconstruction errors between the real surfaces (\mathcal{M}_0 and \mathcal{M}_1) and the reconstructed surfaces ($\widehat{\mathcal{M}}_0$ and $\widehat{\mathcal{M}}_1$).

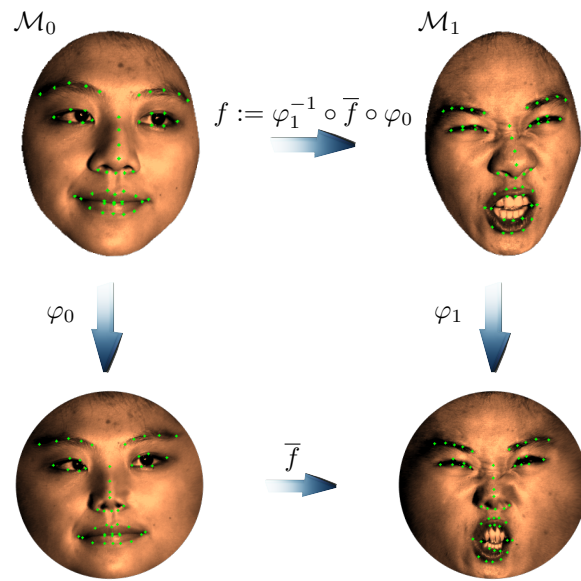


Figure 5: An illustration of the framework for surface registration. The choice of facial landmarks, marked in green, is based on a tree-based shape model [31]. Here \bar{f} is a registration map from $\varphi_0(\mathcal{M}_0)$ to $\varphi_1(\mathcal{M}_1)$, and f is the registration map from \mathcal{M}_0 to \mathcal{M}_1 obtained by $\varphi_1^{-1} \circ \bar{f} \circ \varphi_0$.

corrected by applying a sequence of rigid translations to the 3D surfaces. Algorithms, such as the *iterative closest point* (ICP) [7, 2, 37], can be applied. Finally, a registration map between two normalized 3D surfaces can be computed based on a deformable model between the two surfaces. Since, from Section 2, 3D surfaces can be uniquely represented on the conformal parametric domain \mathbb{D} , in the following, we would like to register two 3D human facial images, \mathcal{M}_0 and \mathcal{M}_1 by computing the deformation map between $\varphi(\mathcal{M}_0)$ and $\varphi(\mathcal{M}_1)$. We assume that the correspondence of the boundary points of \mathcal{M}_0 and \mathcal{M}_1 are known. The assumption can be realized by putting markers on the boundary of the human faces during scanning. We first map each surface conformally to a unit disk \mathbb{D} by using the Riemann mappings

$$\varphi_0 : \mathcal{M}_0 \rightarrow \mathbb{D} \quad \text{and} \quad \varphi_1 : \mathcal{M}_1 \rightarrow \mathbb{D},$$

respectively. Suppose m landmarks are selected manually for each facial expression, due to the bijectivity of the Riemann mapping, we have the corresponding landmark sets on \mathbb{D} , hereafter denoted by $P = \{p^{(i)} \in \mathbb{D}\}_{i=1}^m$ and $Q = \{q^{(i)} \in \mathbb{D}\}_{i=1}^m$, respectively, as illustrated in Figure 5. In the following, we would like to compute the registration maps of MT and DMT via registering the landmark set P and Q , here the DMT registration map is the composition of the Möbius transformation and the elastic deformation field obtained from a modified thin-plate spline model. A brief introduction of the modified thin-plate spline model is introduced in the following.

In the thin-plate model, the deformation field is usually approximated by a linear combination of the biharmonic kernel basis

$$\{\psi_j(x) := r_j(x)^2 \log r_j(x)\}_{j=1}^n$$

at each point in a prescribed set $\mathcal{C} := \{c^{(j)} \in \mathbb{D} \mid c^{(j)} = (c_1^{(j)}, c_2^{(j)})^\top\}_{j=1}^n$, where $r_j(x) := \|x - c^{(j)}\|_0$ is the Euclidean distance between point $c^{(j)}$ and x . Taking the conformal factors into account, we slightly modified the basis function at the point $c^{(j)}$ to be $\tilde{\psi}_j := [\lambda_0^2(c^{(j)})]^{-1} \lambda_1^2(c^{(j)}) \psi_j$, where $\lambda_0(c^{(j)})$ and $\lambda_1(c^{(j)})$ are the conformal factors resulted from the Riemann conformal mappings φ_0 and φ_1 at $c^{(j)}$, respectively, for $j = 1, \dots, n$. Therefore, the registration map \bar{f} of the thin-plate model on \mathbb{D} is defined by $\bar{f}(x) := (\bar{f}_1(x), \bar{f}_2(x))^\top$ with $x = (x_1, x_2)^\top$ and

$$\bar{f}_k(x) = \sum_{j=1}^n \alpha_j^{(k)} \tilde{\psi}_j(x),$$

where $\alpha_j^{(k)}$ are unknown coefficients, for $k = 1, 2$, and $j = 1, \dots, n$. By registering the landmark sets P and Q on \mathbb{D} , these coefficients can be determined by solving the least square problems

$$\min_{\alpha^{(k)}} \left(\sum_{i=1}^m \left\| \bar{f}_k(p^{(i)}) - q^{(i)} \right\|_0^2 \right), \quad k = 1, 2.$$

The least square problems can be easily solved by QR method when $n \leq m$ or solved by Tikhonov regularization [10]

$$(\varepsilon I + S^\top S) \alpha^{(k)} = S^\top q_k$$

when $n > m$, where

$$S_{ij} = \tilde{\psi}_j(p^{(i)}), \quad i = 1, \dots, m, \quad j = 1, \dots, n,$$

$$\alpha^{(k)} = \left(\alpha_1^{(k)}, \dots, \alpha_n^{(k)} \right)^\top, \quad q_k = \left(q_k^{(1)}, \dots, q_k^{(m)} \right)^\top.$$

Then the registration map between \mathcal{M}_0 and \mathcal{M}_1 can be obtained by taking $f = \varphi_1^{-1} \circ \bar{f} \circ \varphi_0$. Figure 6 shows the deformation field of \bar{f} , here the regularization parameter $\varepsilon = 5 \times 10^{-3}$. We measure the correspondence error of the landmark sets on both parametric domain and physical domain by

$$(2) \quad E_{\mathbb{D}}(\bar{f}) = \left(\sum_{i=1}^m \left\| \bar{f}(p^{(i)}) - q^{(i)} \right\|_0^2 \right)^{\frac{1}{2}}.$$

and

$$(3) \quad E(f) = \left(\sum_{i=1}^m \left\| f \circ \varphi_0^{-1}(p^{(i)}) - \varphi_1^{-1}(q^{(i)}) \right\|_0^2 \right)^{\frac{1}{2}},$$

respectively. Table 2 shows the comparison between MT and DMT.

Clearly, from Table 2, one can see that DMT significantly reduces the correspondence errors. This is no surprised by all means since the facial changes are mostly contributed by deformations. Moreover, Figure 6 shows that the deformation map on the parametric domain is smooth without folding and tangling.

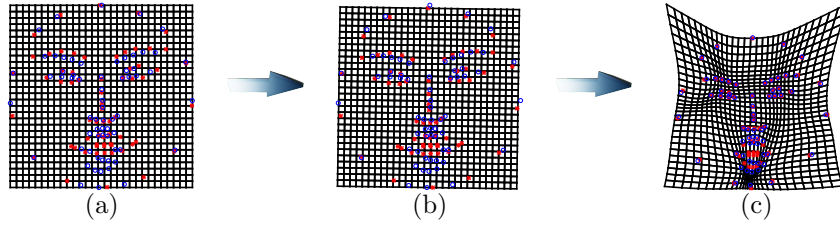


Figure 6: (a) A illustration of the landmark sets P (marked in blue circle) and Q (marked in red asterisk) lay on a checkerboard grid. (b) The registration map via the optimal Möbius transformation (MT). (c) The registration map via composition of MT and the elastic deformation \hat{f} .

registration map	MT	DMT
$E_{\mathbb{D}}(\hat{f})$	1.2559×10^{-1}	6.9174×10^{-2}
$E(f)$	1.2638×10^{-1}	8.2796×10^{-2}

Table 2: A comparison between MT and DMT represented in different error measurements. The measurement $E_{\mathbb{D}}$, defined by (2), measures the distance of each landmark pair on the parametric domain. The measurement E , defined by (3), measures the distance of each landmark pair on the physical domain.

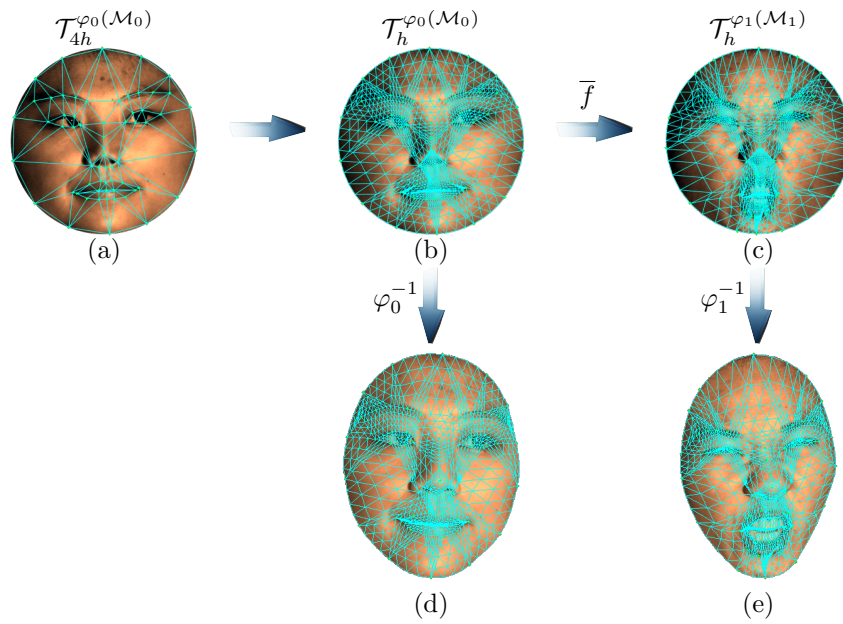


Figure 7: (a) The coarse mesh $\mathcal{T}_{4h}^{\varphi_0}(\mathcal{M}_0)$ of the unit disk $\varphi_0(\mathcal{M}_0)$. (b) A refined mesh of the coarse mesh $\mathcal{T}_{4h}^{\varphi_0}(\mathcal{M}_0)$. (c) The mesh obtained from mapping each vertex of the triangles in $\mathcal{T}_h^{\varphi_0}(\mathcal{M}_0)$ by the registration map \bar{f} . (d) The consistent mesh of the surface \mathcal{M}_0 . (e) The consistent mesh of the surface \mathcal{M}_1 .

4. Surface morphing via consistent meshes and homotopy

In the previous section, we have already obtained a registration map between two surfaces \mathcal{M}_0 and \mathcal{M}_1 . In order to generate a morphing sequence between \mathcal{M}_0 and \mathcal{M}_1 efficiently, we construct a consistent mesh for both \mathcal{M}_0 and \mathcal{M}_1 . First, a coarse mesh, shown in Figure 7, is constructed by connecting the landmarks on the unit disk using straight line segments on $\varphi_0(\mathcal{M}_0)$. Then a finer mesh is obtained by regular mesh refinements for a few times. Let $\mathcal{T}_h^{\varphi_0(\mathcal{M}_0)} = (\mathcal{V}, \mathcal{F})$ denote the final mesh on $\varphi_0(\mathcal{M}_0)$, here \mathcal{V} is the set of all nodal points and \mathcal{F} is the connectivity index set of all triangles. The nodal points in $\mathcal{T}_h^{\varphi_0(\mathcal{M}_0)}$ are mapped to $\varphi_1(\mathcal{M}_1)$ by the registration map \bar{f} . As a result, a mesh on $\varphi_1(\mathcal{M}_1)$ that consists of the mesh on $\varphi_0(\mathcal{M}_0)$, denoted by $\mathcal{T}_h^{\varphi_1(\mathcal{M}_1)}$, can be defined by $\mathcal{T}_h^{\varphi_1(\mathcal{M}_1)} := (\bar{f}(\mathcal{V}), \mathcal{F})$. The detail construction process is shown in the following. Let $(F_i^{(1)}, F_i^{(2)}, F_i^{(3)})$ denote the nodal indices associated with triangle $\tau_i \in \mathcal{T}_h$, for $i = 1, \dots, \#(\mathcal{F})$. Obviously, each point q in triangle τ_i can be represented by

$$q = \beta_{i,1}(q)V_{F_i^{(1)}} + \beta_{i,2}(q)V_{F_i^{(2)}} + \beta_{i,3}(q)V_{F_i^{(3)}},$$

$$\sum_{j=1}^3 \beta_{i,j}(q) = 1, \quad \beta_{i,j}(q) \geq 0, \quad j = 1, 2, 3,$$

where $(\beta_{i,1}(q), \beta_{i,2}(q), \beta_{i,3}(q))$ is the barycentric coordinate of the point q in τ_i . A simple piecewise linear registration map $\bar{f}_{\mathcal{L}} : \varphi_0(\mathcal{M}_0) \rightarrow \varphi_1(\mathcal{M}_1)$, defined as following

$$\bar{f}_{\mathcal{L}}(q) = \beta_{i,1}(q)\bar{f}(V_{F_i^{(1)}}) + \beta_{i,2}(q)\bar{f}(V_{F_i^{(2)}}) + \beta_{i,3}(q)\bar{f}(V_{F_i^{(3)}}), \quad q \in \tau_i,$$

can be employed to approximate the registration map \bar{f} . Similarly, thanks to the (H, λ) unique representation of \mathcal{M} , a piecewise linear approximation $f_{\mathcal{L}}$ of the surface registration map f can also be constructed by

$$f_{\mathcal{L}}(\Psi^{-1}(H_0(q), \lambda_0(q))) := \Psi^{-1}(H_1(\bar{f}_{\mathcal{L}}(q)), \lambda_1(\bar{f}_{\mathcal{L}}(q))), \quad q \in \varphi_0(\mathcal{M}_0).$$

Furthermore, thanks to the conformal parameterization, the registration map between the texture images \mathcal{I}_0 and \mathcal{I}_1 of the surface \mathcal{M}_0 and \mathcal{M}_1 , respectively, can also be approximated by the texture mapping

$$\mathcal{I}_0(\varphi_0^{-1}(q)) \mapsto \mathcal{I}_1(\varphi_1^{-1} \circ \bar{f}_{\mathcal{L}}(q)).$$

In the following, we introduce how we utilize the above consistent mesh to generate the morphing sequence through the cubic spline homotopy of the mean curvatures H_i and the conformal factors λ_i , for $i = 0, 1, \dots, N$. Suppose 3D images of facial expressions $\mathcal{M}_0, \mathcal{M}_1 \dots, \mathcal{M}_N$, are captured at time t_0, t_1, \dots, t_N . Each surface \mathcal{M}_i is mapped to the unit disk \mathbb{D} by the Riemann mapping φ_i , for $i = 0, 1, \dots, N$. Using the above surface registration method, the registration maps

$$(\bar{f}_{\mathcal{L}})_i : \varphi_{i-1}(\mathcal{M}_{i-1}) \rightarrow \varphi_i(\mathcal{M}_i)$$

can be easily computed, for $i = 1, 2, \dots, N$. For convenience, for a given sequence of mappings $\{f_i\}_{i=1}^N$, we define a sequence of composite mappings $\{[f]_i\}_{i=0}^N$ by $[f]_0(q) := q$ and

$$[f]_i := f_i \circ f_{i-1} \circ \dots \circ f_1,$$

for $i = 1, \dots, N$. For each point $q \in \mathbb{D}$, we employ a piecewise cubic spline homotopy to interpolate the data set

$$\{[\bar{f}_{\mathcal{L}}]_0(q), \dots, [\bar{f}_{\mathcal{L}}]_N(q)\}.$$

Let $\mathcal{S}[x_1, \dots, x_n](t)$ denote the piecewise cubic spline function with the given set of data $\{x_1, \dots, x_n\}$. Using the registration maps $\{(\bar{f}_{\mathcal{L}})_i\}_{i=1}^N$, a morphing path $\mathcal{D} : \mathbb{D} \times [t_0, t_N] \rightarrow \mathbb{D}$ on the parametric domain, defined by

$$\mathcal{D}(q, t) = \mathcal{S} [[\bar{f}_{\mathcal{L}}]_0(q), \dots, [\bar{f}_{\mathcal{L}}]_N(q)](t),$$

can be created. Here $\mathcal{D}(q, t)$ denotes the location on the parametric domain where a point $v \in \varphi_0(\mathcal{M}_0)$ is morphed at time t . Since (H, λ) is a unique representation of a surface, the morphing path of $\Psi^{-1}(H, \lambda)$ can also be uniquely determined by the evolution of the conformal factor and the mean curvature. The conformal factor λ and the mean curvature H at $\mathcal{D}(q, t)$ can now be evaluated by

$$H(\mathcal{D}(q, t)) = \mathcal{S} [H_0 \circ [\bar{f}_{\mathcal{L}}]_0(q), \dots, H_N \circ [\bar{f}_{\mathcal{L}}]_N(q)](t)$$

and

$$\lambda(\mathcal{D}(q, t)) = \mathcal{S} [\lambda_0 \circ [\bar{f}_{\mathcal{L}}]_0(q), \dots, \lambda_N \circ [\bar{f}_{\mathcal{L}}]_N(q)](t),$$

respectively. Similarly, suppose the texture images \mathcal{I}_i of the surface \mathcal{M}_i are given, for $i = 0, 1, \dots, N$. The texture image associated with the surface

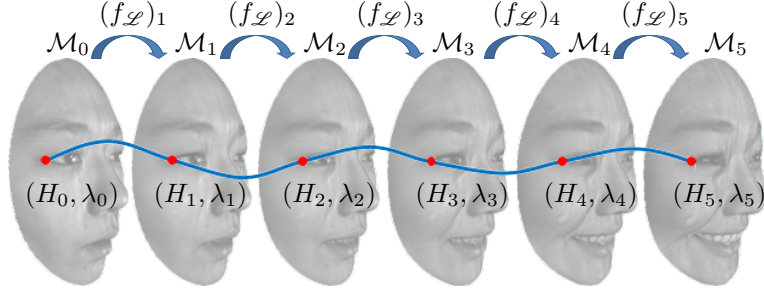


Figure 8: An illustration of the cubic spline homotopy.

along the morphing path $\mathcal{D}(q, t)$ can be computed by the cubic spline homotopy

$$\mathcal{I}_t := \mathcal{S} [\mathcal{I}_0 (\varphi_0^{-1} \circ [\bar{f}_{\mathcal{L}}]_0), \dots, \mathcal{I}_N (\varphi_N^{-1} \circ [\bar{f}_{\mathcal{L}}]_N)] (t).$$

Finally, for any time $t \in [t_0, t_N]$, by reconstructing the 3D surfaces

$$\mathcal{M}_t := \Psi^{-1} (H \circ \mathcal{D}(\mathbb{D}, t), \lambda \circ \mathcal{D}(\mathbb{D}, t))$$

from their (H, λ) representation and by applying the computed texture image \mathcal{I}_t to \mathcal{M}_t , the morphing sequence between \mathcal{M}_0 and \mathcal{M}_N can be obtained. A sketch in Figure 8 illustrates this approach.

5. Numerical results of surface morphing in 3D

In the following, we show some surface morphing results via merely two images by using the surface morphing technique which we have mentioned above. In each demonstration, shown in Figure 9, the landmarks on each surface are manually selected. The leftmost image is the role of initial surface \mathcal{M}_0 while the rightmost image is the role of terminal surface \mathcal{M}_1 , and the images in the middle are the morphing sequence between \mathcal{M}_0 and \mathcal{M}_1 .

It is interesting that how much DMT improves the morphing sequence. For this purpose, we captured a 3D video of little movements on human face. The captured surface at time t is denoted by \mathcal{M}_t , for $t \in [0, 2]$. Then we construct the morphing sequence via 3 key frames $\{\mathcal{M}_t | t = 0, 1, 2\}$. The registration map constructed by using MT and DMT are denoted by $(\bar{f}_{\mathcal{L}}^{\text{MT}})_i$ and $(\bar{f}_{\mathcal{L}}^{\text{DMT}})_i$, respectively, for $i = 1, 2$. In order to measure the rate of improvement, we reconstruct the surfaces $\widehat{\mathcal{M}}_t^{\text{MT}} := \Psi^{-1} (H_t^{\text{MT}}, \lambda_t^{\text{MT}})$ and

$\widehat{\mathcal{M}}_t^{\text{DMT}} := \Psi^{-1}(H_t^{\text{DMT}}, \lambda_t^{\text{DMT}})$ where

$$H_t^{\text{MT}} := \mathcal{S} \left[H_0 \circ \left[\overline{f}_{\mathcal{L}}^{\text{MT}} \right]_0, \dots, H_2 \circ \left[\overline{f}_{\mathcal{L}}^{\text{MT}} \right]_2 \right] (t),$$

$$\lambda_t^{\text{MT}} := \mathcal{S} \left[\lambda_0 \circ \left[\overline{f}_{\mathcal{L}}^{\text{MT}} \right]_0, \dots, \lambda_2 \circ \left[\overline{f}_{\mathcal{L}}^{\text{MT}} \right]_2 \right] (t),$$

$$H_t^{\text{DMT}} := \mathcal{S} \left[H_0 \circ \left[\overline{f}_{\mathcal{L}}^{\text{DMT}} \right]_0, \dots, H_2 \circ \left[\overline{f}_{\mathcal{L}}^{\text{DMT}} \right]_2 \right] (t),$$

and

$$\lambda_t^{\text{DMT}} := \mathcal{S} \left[\lambda_0 \circ \left[\overline{f}_{\mathcal{L}}^{\text{DMT}} \right]_0, \dots, \lambda_2 \circ \left[\overline{f}_{\mathcal{L}}^{\text{DMT}} \right]_2 \right] (t),$$

for $t \in [0, 2]$. Then, we compute the relative surface difference

$$\|\mathcal{M}_t - \widehat{\mathcal{M}}_t^{\text{MT}}\|_2 := \left(\frac{\iint_{\mathbb{D}} \|\mathcal{M}_t(u_1, u_2) - \widehat{\mathcal{M}}_t^{\text{MT}}(u_1, u_2)\|_0^2 \left| \frac{\partial \varphi^{-1}}{\partial u_1} \wedge \frac{\partial \varphi^{-1}}{\partial u_2} \right| du_1 du_2}{\iint_{\mathbb{D}} \left| \frac{\partial \varphi^{-1}}{\partial u_1} \wedge \frac{\partial \varphi^{-1}}{\partial u_2} \right| du_1 du_2} \right)^{\frac{1}{2}},$$

and

$$\|\mathcal{M}_t - \widehat{\mathcal{M}}_t^{\text{DMT}}\|_2 := \left(\frac{\iint_{\mathbb{D}} \|\mathcal{M}_t(u_1, u_2) - \widehat{\mathcal{M}}_t^{\text{DMT}}(u_1, u_2)\|_0^2 \left| \frac{\partial \varphi^{-1}}{\partial u_1} \wedge \frac{\partial \varphi^{-1}}{\partial u_2} \right| du_1 du_2}{\iint_{\mathbb{D}} \left| \frac{\partial \varphi^{-1}}{\partial u_1} \wedge \frac{\partial \varphi^{-1}}{\partial u_2} \right| du_1 du_2} \right)^{\frac{1}{2}},$$

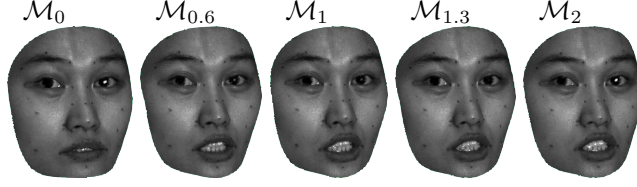
The rate of improvement is defined by

$$(4) \quad \text{Rate}_t := \frac{\|\mathcal{M}_t - \widehat{\mathcal{M}}_t^{\text{MT}}\|_2 - \|\mathcal{M}_t - \widehat{\mathcal{M}}_t^{\text{DMT}}\|_2}{\|\mathcal{M}_t - \widehat{\mathcal{M}}_t^{\text{MT}}\|_2}.$$

Table 3 indicates that DMT improves approximately 50% of the surface difference.

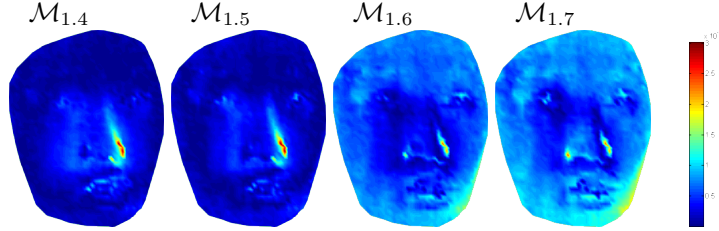
Moreover, extrapolation can also be achieved by using this homotopy technique. In the following numerical experiment, the real surface at time t is denoted by \mathcal{M}_t and the reconstructed surface at time t is denoted by $\widehat{\mathcal{M}}_t := \Psi^{-1}(H_t, \lambda_t)$ where

$$H_t := \mathcal{S} \left[H_{0.6}, H_1 \circ \left[\overline{f}_{\mathcal{L}}^{\text{DMT}} \right]_1, H_{1.3} \circ \left[\overline{f}_{\mathcal{L}}^{\text{DMT}} \right]_2 \right] (t)$$



t	$\ \mathcal{M}_t - \widehat{\mathcal{M}}_t^{\text{MT}}\ _2$	$\ \mathcal{M}_t - \widehat{\mathcal{M}}_t^{\text{DMT}}\ _2$	Rate $_t$
0.3	1.4980×10^{-2}	8.6761×10^{-3}	42.08%
0.4	2.0554×10^{-2}	1.1229×10^{-2}	45.37%
0.5	2.3328×10^{-2}	1.0679×10^{-2}	54.22%
1.3	4.1535×10^{-2}	1.8688×10^{-2}	55.01%
1.4	3.9139×10^{-2}	1.9036×10^{-2}	51.36%

Table 3: A comparison between MT and DMT represented in different error measurements. Here Rate $_t$, defined by (4), is the rate of improvement.



t	$\ \mathcal{M}_t - \widehat{\mathcal{M}}_t\ _2$	$\ \mathcal{M}_t - \widehat{\mathcal{M}}_t\ _\infty$
1.4	1.3639×10^{-2}	8.7590×10^{-2}
1.5	1.2816×10^{-2}	9.0388×10^{-2}
1.6	2.6365×10^{-2}	7.1989×10^{-2}
1.7	3.2057×10^{-2}	7.1733×10^{-2}

Table 4: The extrapolation error between the real surface and the reconstructed surface represented in different error measurements.

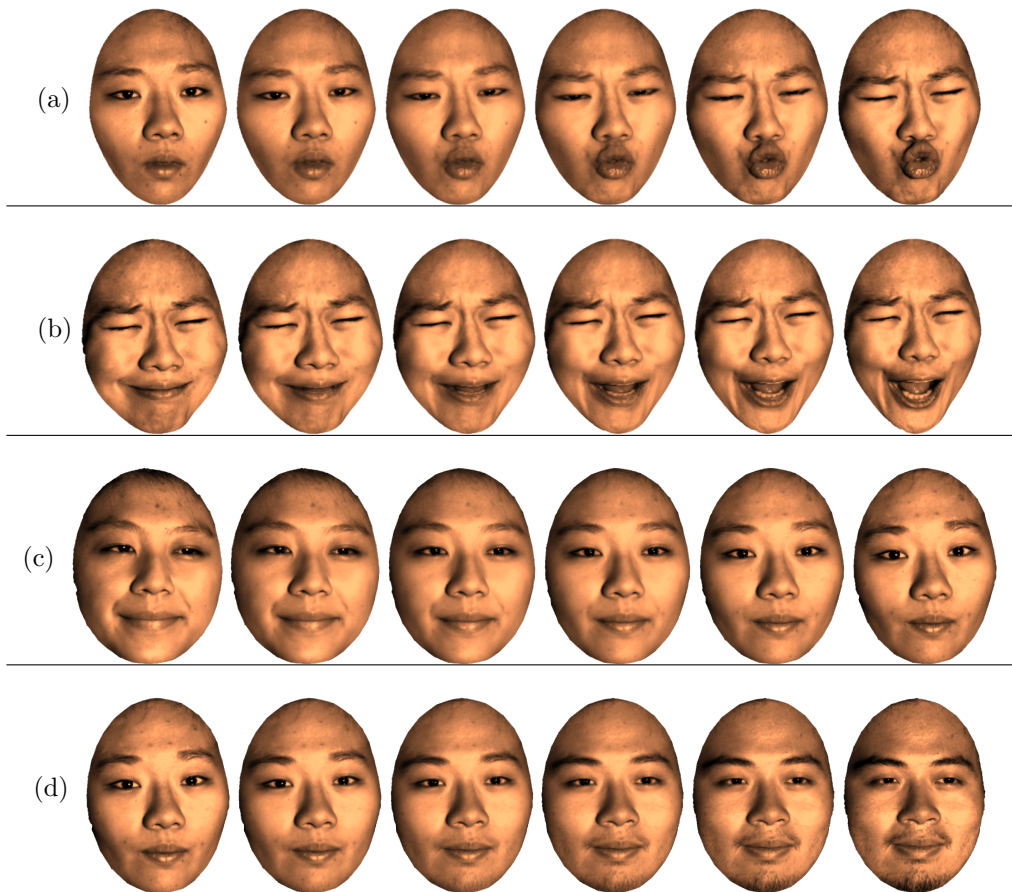


Figure 9: (a) A morphing sequence of an eye blinking motion of a girl. (b) A morphing sequence of a mouth opening motion of a girl. (c) A morphing sequence of a face transformation from a girl's face into another girl's face. (d) A morphing sequence of a face transformation from a girl's face into a boy's face.

and

$$\lambda_t := \mathcal{S} \left[\lambda_{0.6}, \lambda_1 \circ \left[\overline{f}_{\mathcal{L}}^{\text{DMT}} \right]_1, \lambda_{1.3} \circ \left[\overline{f}_{\mathcal{L}}^{\text{DMT}} \right]_2 \right] (t).$$

Table 4 shows the relative surface difference between the real surface \mathcal{M}_t and the reconstructed surface $\widehat{\mathcal{M}}_t := \Psi^{-1}(H_t, \lambda_t)$ in L^2 -norm

$$\|\mathcal{M}_t - \widehat{\mathcal{M}}_t\|_2 := \left(\frac{\iint_{\mathbb{D}} \|\mathcal{M}_t(u_1, u_2) - \widehat{\mathcal{M}}_t(u_1, u_2)\|_0^2 \left| \frac{\partial \varphi^{-1}}{\partial u_1} \wedge \frac{\partial \varphi^{-1}}{\partial u_2} \right| du_1 du_2}{\iint_{\mathbb{D}} \left| \frac{\partial \varphi^{-1}}{\partial u_1} \wedge \frac{\partial \varphi^{-1}}{\partial u_2} \right| du_1 du_2} \right)^{\frac{1}{2}},$$

and in L^∞ -norm

$$\|\mathcal{M}_t - \widehat{\mathcal{M}}_t\|_\infty := \max_{(u_1, u_2) \in \mathbb{D}} \left\| \mathcal{M}_t(u_1, u_2) - \widehat{\mathcal{M}}_t(u_1, u_2) \right\|_0,$$

at time $t = 1.4, 1.5, 1.6$ and 1.7 , respectively.

6. Conclusion

In this paper, we proposed a 3D surface morphing method for simply connected surfaces with a single boundary in which smooth transitions on both geometric characteristics and texture of the surfaces are considered. Similar to the traditional morphing approaches based on boundary representation, a wrap has to be created via the feature correspondence and interpolation between shapes based on the wrap is employed to generate the morphing sequence. By taking the advantages of the conformal parameterization and the unique surface representation of the conformal factor and the mean curvature, the wrap can be easily obtained by the composition of deformations from the Möbius transformation and the thin-plate registration function. To mimic the non-isomorphic risk that usually occurs in registering largely deformed surfaces, a consistent mesh based on wrapping is employed. As a result, the correspondence, including geometric information and texture information, of the whole surface can be defined and interpolation among the source surface and the target surface can be computed by the usual cubic spline homotopy on a disk parametric domain. Finally, the morphing sequence can be generated from the surface reconstruction algorithm in section 2.2. To make the proposed morphing approach more attractive in real applications, we improve the efficiency in computing the conformal parameterization. Also, we propose a nonlinear iterative surface reconstruction algorithm (Algorithm 1) that can be accelerated by using the multigrid

method on a consistent mesh by which multi-resolution surfaces can also be obtained. Several morphing results among different 3D facial expressions are presented to demonstrate the feasibility of the proposed surface morphing method.

References

- [1] Y. Bao, X. Guo, and H. Qin. Physically based morphing of point-sampled surfaces. *Computer Animation and Virtual Worlds*, 16:509–518, 2005.
- [2] P. J. Besl and N. D. McKay. A method for registration of 3-d shapes. *IEEE Trans. on Pattern Analysis and Machine Intelligence*, 14(2):239–256, 1992.
- [3] F. L. Bookstein. Principal warps: Thin-plate splines and the decomposition of deformations. *IEEE Transactions on Pattern Analysis and Machine Intelligence*, 11(6):567–585, 1989.
- [4] V. Camion and L. Younes. Geodesic interpolating splines. *Energy Minimization Methods in Computer Vision and Pattern Recognition, Lecture notes in Computer Science*, 2134:513–527, 2001.
- [5] Y. Cao, M. I. Miller, R. L. Winslow, and L. Younes. Large deformation diffeomorphic metric mapping of vector fields. *IEEE Transactions on Medical Imaging*, 24(9):1216–1230, 9 2005.
- [6] R. Chen, O. Weber, D. Keren, and M. Ben-Chen. Planar shape interpolation with bounded distortion. *ACM Trans. Graph.*, 32(4):108:1–108:12, July 2013.
- [7] Y. Chen and G. Medioni. Object modelling by registration of multiple range images. *Image Vision Comput.*, pages 145–155, 1991.
- [8] T. F. Cootes, C. J. Taylor, D. H. Cooper, and J. Graham. Active shape models - their training and application. *Computer Vision and Image Understanding*, 61(1), 1995.
- [9] D. DeCarlo, D. Metaxas, and & M. Stone. An anthropometric face model using variational techniques. *In Proceedings of the 25th annual conference on Computer graphics and interactive techniques. ACM.*, pages 67–74, July 1998.
- [10] H. W. Engl, M. Hanke, and A. Neubauer. *Regularization of Inverse Problems*. Kluwer Academic Publishers, 1 edition, 1996.

- [11] O. Forster. *Lectures on Riemann Surfaces*. Springer, 2005.
- [12] A. Gregory, A. State, M. C. Lin, D. Manocha, and M. A. Livingston. Interactive surface decomposition for polyhedral morphing. *The Visual Computer*, 15:453–470, 1999.
- [13] X. Gu, T.-M. Huang, W.-Q. Huang, S.-S. Lin, W.-W. Lin, and S.-T. Yau. High performance computing for spherical conformal and Riemann mappings. *Geometry, Imaging and Computing*, 1(2):223–258, 2014.
- [14] X. Gu and B. C. Vemuri. Matching 3d shapes using 2d conformal representations. *Medical Image Computing and Computer-Assisted Intervention V MICCAI 2004*, 3216:771–780, 2004.
- [15] X. Gu, Y. Wang, T. F. Chan, P. M. Thompson, and S.-T. Yau. Genus zero surface conformal mapping and its application to brain surface mapping. *IEEE Transactions on Medical Imaging*, 8, 2004.
- [16] X. Gu, Y. Wang, and S.-T. Yau. Geometric compression using riemann surface structure. *Communications in Information and Systems*, 3:171–182, 2004.
- [17] X. Gu and S.-T. Yau. *Computational Conformal Geometry*. Higher Education Press, 1 edition, 2008.
- [18] E. Jeong, M. Yoon, Y. Lee, M. Ahn, S. Lee, and B. Guo. Feature-based surface light field morphing. *Proceedings of the 11th Pacific Conference on Computer Graphics and Applications*, pages 215–223, 2003.
- [19] J. Jost. *Compact Riemann Surfaces*. Springer-Verlag Berlin Heidelberg, 3 edition, 2006.
- [20] S. Kurtek, A. Srivastava, E. Klassen, and H. Laga. Landmark-guided elastic shape analysis of spherically-parameterized surfaces. *Computer Graphics Forum*, 32(2pt4):429–438, 2013.
- [21] S.-Y. Lee, K.-Y. Chwa, J. Hahn, and S. Y. Shin. Image morphing using deformable surfaces. *Proceedings of Computer Animation*, pages 31–39, 1994.
- [22] Y. Lipman and T. Funkhouser. Möbius voting for surface correspondence. *ACM Transactions on Graphics (Proc. SIGGRAPH)*, 28(3), August 2009.
- [23] N. Litke, M. Droske, M. Rumpf, and P. Schröder. An image processing approach to surface matching. In *Proceedings of the Third Euro-*

graphics Symposium on Geometry Processing, SGP '05, Aire-la-Ville, Switzerland, Switzerland, 2005. Eurographics Association.

- [24] Y.-S. Liu, H.-B. Yan, and R. R. Martin. As-rigid-as-possible surface morphing. *Journal of Computer Science and Technology*, 26:548–557, 2011.
- [25] W. C. Ma, A. Jones, J. Y. Chiang, T. Hawkins, S. Frederiksen, P. Peers, M. Vukovic, M. Ouhyoung, and P. Debevec. Facial performance synthesis using deformation-driven polynomial displacement maps. *ACM Transactions on Graphics*, 2008.
- [26] A. B. Mattos, J. P. Mena-Chalco, and R. M. Cesar Jr. 3d facial animation based on structural registration. *Workshops of Sibgrapi 2009-Posters*, 2009.
- [27] M. Meyer, M. Desbrun, P. Schröder, and A. H. Barr. Discrete differential-geometry operators for triangulated 2-manifolds. In *Visualization and mathematics III*, pages 35–57. Springer, 2003.
- [28] M. Obaid, R. Mukundan, M. Billinghurst, and C. Pelachaud. Expressive MPEG-4 facial animation using quadratic deformation models. In *Computer Graphics, Imaging and Visualization (CGIV), 2010 Seventh International Conference on. IEEE.*, pages 9–14, August 2010.
- [29] H. Poincaré. Sur l’uniformisation des fonctions analytiques. *Acta Mathematica*, 31(1):1–63, 1908.
- [30] D. Smythe. A two-pass mesh warping algorithm for object transformation and image interpolation. 1990.
- [31] Michal Uříčář, Vojtěch Franc, and Václav Hlaváč. Facial Landmark Tracking by Tree-Based Deformable Part Model Based Detector. In *The IEEE International Conference on Computer Vision (ICCV) Workshops*. IEEE, December 2015.
- [32] L. J. van Vliet and P. W. Verbeek. Curvature and bending energy in 2d and 3d images. *Scandinavian Conference on Image Analysis*, 2:1403–1410, 1993.
- [33] G. Wolberg. Recent advances in image morphing. *IEEE Proceedings in Computer Graphics International*, 1996.
- [34] G. Wolberg. Image morphing: a survey. *The Visual Computer*, 14(8):360–372, 1998.

- [35] M. Yang, K. Wang, and L. Zhang. Realistic real-time facial expressions animation via 3d morphing target. *Journal of Software*, 8(2), 2013.
- [36] V. Zanella, G. Ramirez, H. Vargas, and L. V. Rosas. Automatic morphing of face images. In *Adaptive and Natural Computing Algorithms*, volume 5495 of *Lecture Notes in Computer Science*, pages 600–608. Springer Berlin Heidelberg, 2009.
- [37] Z. Zhang. Iterative point matching for registration of free-form curves and surfaces. *International Journal of Computer Vision*, 13(12):119–152, 1994.

MEI-HENG YUEH

E-mail address: mhyueh@math.nctu.edu.tw

XIANFENG DAVID GU

E-mail address: gu@cs.sunysb.edu

WEN-WEI LIN

E-mail address: wmlin@math.nctu.edu.tw

CHIN-TIEN WU

E-mail address: ctw@math.nctu.edu.tw

SHING-TUNG YAU

E-mail address: yau@math.harvard.edu